

## REPORT DOCUMENTATION PAGE

AFRL-SR-AR-TR-09-0311

The public reporting burden for this collection of information is estimated to average 1 hour per response, including the time for review, maintaining the data needed, and completing and reviewing the collection of information. Send comments regarding this burden estimate, suggestions for reducing the burden, to the Department of Defense, Executive Service Directorate (0704-0188). Respondents should be aware that no person shall be subject to any penalty for failing to comply with a collection of information if it does not display a currently valid OMB control number.

**PLEASE DO NOT RETURN YOUR FORM TO THE ABOVE ORGANIZATION.**

1. REPORT DATE (DD-MM-YYYY) 25-09-2009		2. REPORT TYPE Final		3. DATES COVERED (From - To) 1-02-2006 - 30-05-2009	
4. TITLE AND SUBTITLE High Frequency Combustion Instability Studies of LOX/Methane Fueled Rocket Engines				5a. CONTRACT NUMBER FA9550-06-1-0151	
				5b. GRANT NUMBER	
				5c. PROGRAM ELEMENT NUMBER	
				5d. PROJECT NUMBER	
6. AUTHOR(S) Santoro, Robert, J.				5e. TASK NUMBER	
				5f. WORK UNIT NUMBER	
7. PERFORMING ORGANIZATION NAME(S) AND ADDRESS(ES) The Pennsylvania State University, University Park, PA				8. PERFORMING ORGANIZATION REPORT NUMBER	
9. SPONSORING/MONITORING AGENCY NAME(S) AND ADDRESS(ES) Air Force Office of Scientific Research 875 N. Randolph St. Arlington, VA 22203				10. SPONSOR/MONITOR'S ACRONYM(S) AFOSR	
				11. SPONSOR/MONITOR'S REPORT NUMBER(S)	
12. DISTRIBUTION/AVAILABILITY STATEMENT Unclassified, Unlimited					
13. SUPPLEMENTARY NOTES					
14. ABSTRACT A series of studies were conducted using a rectangular rocket chamber burning LOX/methane propellants to investigate the effect of the temperature of the methane on the initiation of combustion instability. The rectangular rocket used in these studies employed LOX centered coaxial swirl injectors. The rectangular injector used in these studies provided 16 possible injector element locations in a linear array. Variation of injector element location showed that injector elements placed near the pressure anti-node of the first transverse acoustic mode of the chamber resulted in higher pressure oscillations than injector elements located near the pressure node of this mode. The methane propellant temperature varied over a temperature range from -70 to -100°F (-56 to -73°C) for the cooled studies and from -6 to +40°F (-21 to +4°C) for the ambient temperature studies. The results obtained from monitoring the pressure oscillations using high-speed pressure transducers indicated no difference between the cooled methane test cases as compared to the ambient temperature test cases.					
15. SUBJECT TERMS combustion instability, rockets, methane, liquid oxygen					
16. SECURITY CLASSIFICATION OF:			17. LIMITATION OF ABSTRACT	18. NUMBER OF PAGES 28	19a. NAME OF RESPONSIBLE PERSON
a. REPORT	b. ABSTRACT	c. THIS PAGE			Robert J. Santoro
U	U	U	UU		19b. TELEPHONE NUMBER (include area code) 814-863-1285

20091116196

Reset

Standard Form 298 (Rev. 8/98)  
Prescribed by ANSI Std. Z39.18  
Adobe Professional 7.0

## TABLE OF CONTENTS

Executive Summary	3
1.0 Introduction	4
2.0 Objectives	5
3.0 Experimental Setup	6
3.1 The Cryogenic Combustion Laboratory	6
3.2 Experimental Hardware	7
3.2.1 Main Chamber Design	7
3.2.2 Injector and Injector Block	8
3.2.3 Propellant Manifold	9
3.2.4 Nozzle and Nozzle Block	11
3.2.5 Igniters	11
3.2.6 High Frequency Pressure Transducers	11
3.3 Test Conditions	12
3.3.1 Basic Flow Conditions	12
3.3.2 Basic Timing Sequence	13
4.0 Results and Discussion	13
4.1 High Frequency Data Analysis Overview	13
4.1.1 Chamber Acoustic Characteristics	13
4.1.2 Power Spectrum Density Overview	15
4.1.3 Power Spectrum Density Analysis	16
4.2 Chamber Response	17
4.2.1 Acoustic Response Studies	17
4.2.2 Burst Phenomenon	19
4.2.3 Short-Time Fourier Analysis	20
4.2.4 Temperature Ramping Studies	22
5.0 Summary and Conclusions	25
6.0 References	26
7.0 Personnel Supported	27
8.0 Publications	27
9.0 Interactions/Transitions	28
9.1 Participation/presentation at meeting, conferences, workshops and seminars, etc.	28
9.2 Consultative and advisory functions to other laboratories and agencies	28
9.3 New discoveries, inventions and patent disclosures	28
10.0 Honors/Awards	28

### **Executive Summary**

A series of studies were conducted using a rectangular rocket chamber burning LOX/methane propellants to investigate the effect of the temperature of the methane on the initiation of combustion instability. The rectangular rocket used in these studies employed LOX centered coaxial swirl injectors. The rectangular injector used in these studies provided 16 possible injector element locations in a linear array. Variation of injector element location showed that injector elements placed near the pressure anti-node of the first transverse acoustic mode of the chamber resulted in higher pressure oscillations than injector elements located near the pressure node of this mode. The methane propellant temperature varied over a temperature range from -70 to -100°F (-56 to -73°C) for the cooled studies and from -6 to +40°F (-21 to +4°C) for the ambient temperature studies. The results obtained from monitoring the pressure oscillations using high-speed pressure transducers indicated no difference between the cooled methane test cases as compared to the ambient temperature test cases.

## 1.0 Introduction

Combustion instability is well recognized as a major risk in rocket engine development programs, particularly for liquid propellant rocket engines. Occurrences of combustion instability events have been observed in numerous engine development programs dating from the early 1950's. Particularly troubling is that no fundamentally based design methodology for predicting the onset and sustenance of combustion instability in rocket engines exists. Furthermore, because chamber size is important in defining the acoustic modes of the chamber, incidences of unstable behavior are often not observed until the full scale engine is tested, usually near the final stage of the program. From a cost and schedule perspective, this is the worst engine scale at which to address a critical problem that places the entire development program at risk.

A major reason for the lack of a fundamental understanding of combustion instability is due to the complexity and multi-variable nature of the phenomena itself. Initiation and sustenance of combustion instability has been shown to be sensitive to a number of potential driving mechanisms including propellant injection, inter-element injector flow interactions, atomization to form drops, secondary atomization of drops, drop heating and vaporization, mixing processes involving the drops and gases, mixture ratio distribution in space and time, chemical reaction and gas dynamics. Different stability behavior is also seen for different propellant combinations (e.g. liquid oxygen/hydrogen (LOX/H<sub>2</sub>), LOX/kerosene, storables, etc.) as well as for different injector geometries (shear coaxial, swirl coaxial, impinging jet, pintle, etc.). Thus, it is not clear that a single mechanism is responsible for the occurrence of combustion instability in every rocket engine in which combustion instability is reported or whether multiple mechanisms are concurrently present. One observation is clear, it is rare for a rocket engine development program to not experience rocket instability problems, and the current understanding to address such problems is largely empirical in nature. It is also clear that analysis capabilities to understand the initiation and sustenance of combustion instability must be improved if high performance reliable rocket engines are to be developed in a cost effective manner. Furthermore, it can be stated that gaining this needed capability will not result from a single research effort but will rather only be achieved by a systematic series of studies that investigate the underlying fundamental processes that drive combustion instability. The overriding objective is to have a continuing improved understanding of combustion



instability such that the best possible tools are available when rocket instability problems arise. Ultimately, one would like to have a comprehensive understanding of combustion instability, but history has shown that such an understanding is elusive. Yet, with each study, new key understanding is gained that contributes to achieving the desired goal of a comprehensive model that provides a design methodology to avoid occurrences of combustion instability.

Given the ubiquitous nature of the occurrence of combustion instability in liquid propellant rocket engines, nearly every review of critical areas for which improved understanding is required, ranks it at or near the top for needed future work [1]. Historically, combustion instability has been most problematic for LOX/hydrocarbon (particularly kerosene) and storable propellants such as nitrogen tetroxide in combination with the hydrazine family of fuels. Engines using LOX/H<sub>2</sub> propellants have experienced considerably less incidences of combustion instability, but are not totally immune to such problems [2, 3]. However the use of liquid hydrogen introduces serious systems related issues due to its low density leading to large fuel tanks and its low vaporization temperature limiting its storability. Recently, renewed interest in lower operational costs, higher propellant density and less challenging thermal storability has renewed interest in methane as a fuel to be used with LOX. Methane offers the advantage of being a "soft cryogen" as its vaporization temperature is significantly higher than that of liquid hydrogen (-259°F (111.7 K) vs. -423°F (20 K)). Thus, both the Air Force and NASA are looking towards LOX/methane for upper stage and in-space propulsion applications.

Given this recent interest in the LOX/methane propellant combination, the present study focuses on combustion instability in LOX/methane systems. In particular, emphasis was given to investigating the effects of fuel temperature on the onset of combustion instability for a generic set of injector element types.

## **2.0 Objectives**

The overarching objective of the proposed research program was to advance our understanding of the initiation and sustenance of combustion instability in rocket engines that use a liquid oxygen/methane propellant combination. Utilizing an existing multi-element test chamber that is described in the next sub-section, we propose to focus on the following set of specific objectives:

- [1] To determine the chamber pressure and fuel temperature at which the onset of transverse modes due to combustion instability are observed to occur for subcritical, transcritical and supercritical propellant conditions for three representative injector element types.
- [2] To determine a pressure scaling relationship for each injector element for the onset of combustion instability based on measurements done over a range of discrete chamber pressures and propellant temperature conditions.
- [3] To establish a baseline set of data to characterize combustion instability for injectors which operate over a 10:1 throttling range.
- [4] To transfer the understanding gained in this research program rapidly to industry through close cooperation with the leading U.S. liquid propellant rocket manufacturer, Pratt and Whitney.

### **3.0 Experimental Setup**

#### **3.1 The Cryogenic Combustion Laboratory**

A series of combustion instability studies were conducted at the Cryogenic Combustion Laboratory (CCL). Several publications contain information regarding the layout and capabilities of the CCL [4-8]. Thus, only an overview of the facilities will be discussed here. The CCL facility consists of three rooms constructed with reinforced concrete to protect operators and adjacent areas from any hazardous explosions or conditions which may occur. The main room is the control room, which holds the data acquisition computers and flow control equipment. A programmable logic controller (PLC) remotely actuates valves and monitors critical pressure transducers in the flow system. If a pressure transducer or other sensor reads outside of programmed ranges, an abort monitor automatically aborts the test and brings on purge gases to purge the system of combustible propellants. The control room also houses various PC computers and timing systems used for data acquisition. One dedicated computer located at the control panel provides the operators with real time data overviews and data acquisition status. Other computers are used for other acquisition tasks, so that critical performance data (pressure and temperature) may be taken separately from other advanced diagnostics (laser based techniques, high frequency pressure measurements, etc.). A separate instrumentation room houses lasers, optics, and any other equipment needed for data capture

during a test which is deemed too fragile to leave next to the rocket should a hardware failure occur. Optical and cable access ports are available to route the necessary equipment or sensors into the test cell for data capture.

Flowrate capabilities at the CCL provide 0.45 kg/s (1.0 lbm/s) of liquid and gaseous oxygen (LOX and GOX), 0.11 kg/s (0.25 lbm/s) of gaseous hydrogen ( $\text{GH}_2$ ), 0.23 kg/s (0.50 lbm/s) of liquid hydrocarbon (methanol, RP-1, etc.), and 2.27 kg/s (5.0 lbm/s) of air. Propellant flowrate control is accomplished using critical orifices for gaseous flow and cavitating venturis for liquid flows.

### 3.2 Experimental Hardware

#### 3.2.1 Main Chamber Design

Experiments for studies discussed in this report were conducted in a multi-element, rectangular rocket chamber. Propellants chosen for these studies were liquid oxygen (LOX) and gaseous methane ( $\text{CH}_4$ ). Figure 1 shows a schematic of the rocket chamber on the test stand whereas Fig. 2 shows an overhead photograph of the rocket on the test stand. Flow is from top to bottom in the picture. When assembled, the combustion chamber measures 203 mm (8.00 in.) wide by 81.3 mm (3.20 in.) long (in the flow direction) by 19 mm (0.75 in.) high. These

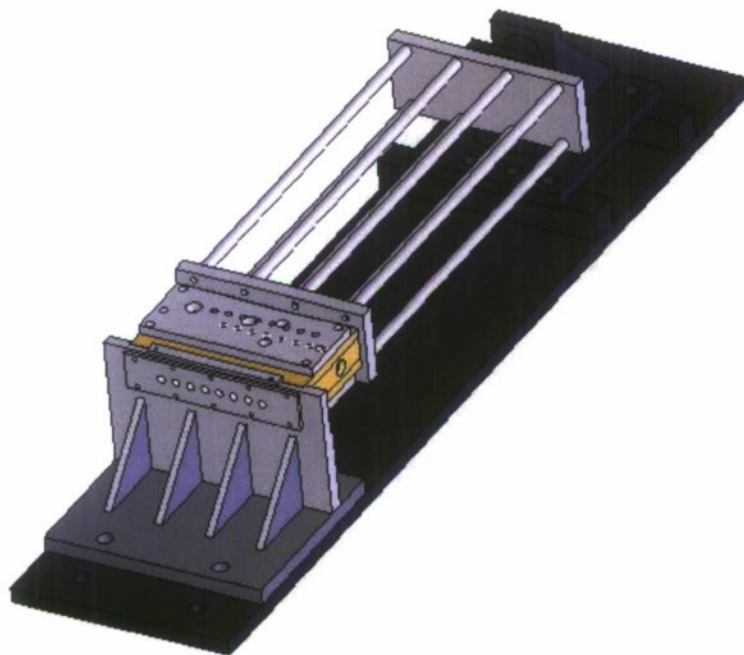
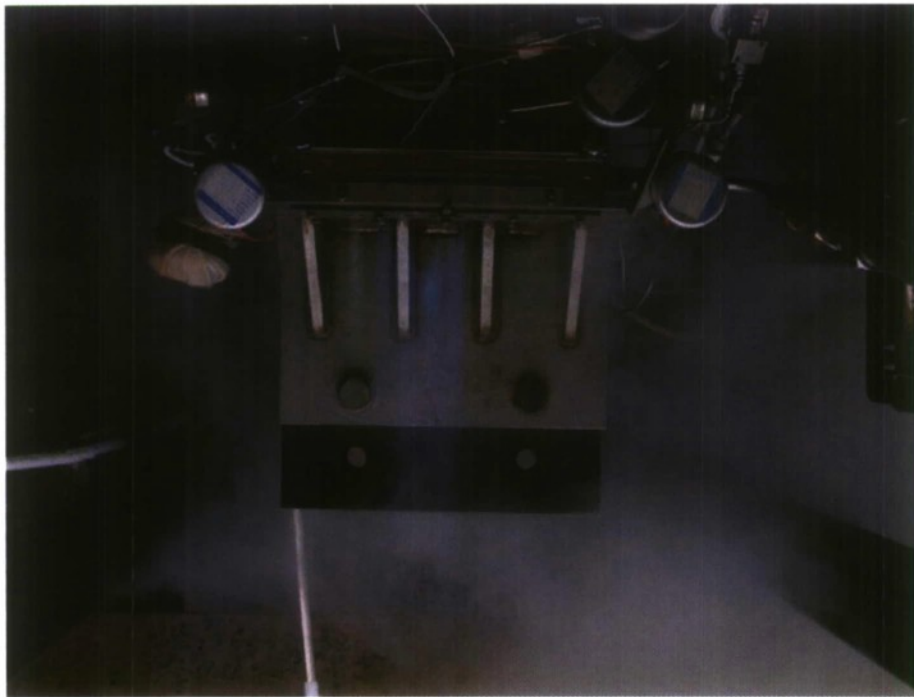


Fig. 1. Schematic of rectangular chamber on test stand.





**Fig. 2.** Photograph of rocket firing (2 injectors, 8 nozzles,  $P_c=222$  psia,  $O/F=3$ ). Flow is from top to bottom in the photograph.

dimensions were chosen to isolate the first and second transverse modes (1W and 2W modes) of the chamber at frequencies low enough ( $\sim 2000$ -8000 Hz) to be readily studied. At the head end of the chamber is located an injector body with ports for up to 16 injector elements. At the exhaust end of the chamber, a nozzle body is located with ports for up to 8 nozzle elements. Each injector element and nozzle element could be independently moved within the injector body and nozzle body, respectively. Injector/nozzle element refers to a single injector/nozzle, whereas injector/nozzle body (or block) refers to the component that holds several injector/nozzle elements or their blanks, and is multi-element in nature. For discussion throughout the report, the injectors and nozzles have been numbered for clarity. Figure 3 shows a section view of the chamber with injector and nozzle elements numbered and the igniter ports and water passage ports identified

### 3.2.2 Injector and Injector Block

The primary injector element design utilized in the majority of studies was a swirl coaxial injector. The swirl coaxial injector element consisted of a central post through which LOX was introduced. At one end of the post was a swirl nut. The ID of the post was 2.36 mm (0.093 in.)



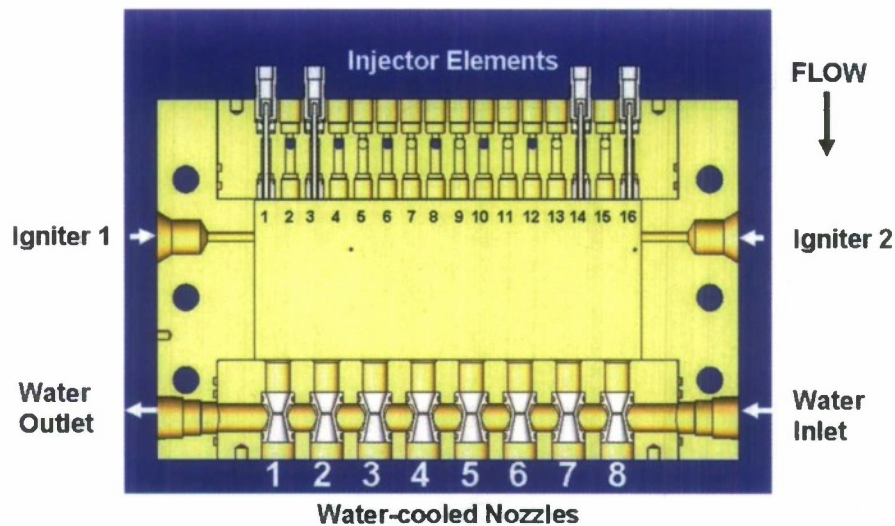


**Fig. 3.** Section view of chamber with injector elements and nozzle elements numbered.

while its OD was 3.30 mm (0.130 in.): The post length was 50.8 mm (2.00 in.) from the end of the swirl nut to the injection plane. Six tangential holes 0.79 mm (1/32 in.) in diameter were located in the swirl nut. The holes were biased three to a side, mirrored about the central axis of the post, in order to introduce a radial component to the flow. The injector post was silver soldered into a custom made fitting which was used to insert the injector element into the injector body. The fuel annulus was formed by an insert on the injection side of the injector body. The primary injector element annulus insert was 3.91 mm (0.154 in.) outer diameter. Centering rings located between the annulus insert and injector body kept the LOX post aligned. Stand-offs of various lengths could be inserted into the upstream side of the injector body to produce various LOX post recesses. For the experiments discussed here, all stand-offs were 5.08 mm (0.200 in.) in length to produce a flush injector face. A schematic of the injector element is shown in Fig. 4 and a cut-away schematic showing the assembly of four injector elements in the injector body is shown in Fig. 5.

### 3.2.3 Propellant Manifold

To ensure single phase liquid flow, the LOX feed lines were jacketed and cooled with LN<sub>2</sub>. Prior to connecting with the injector block, the LOX manifold is submerged in a LN<sub>2</sub> bath with independent feed lines from the manifold connecting to injector elements. Each independent feed line also has a LN<sub>2</sub> jacket to keep propellants at cryogenic temperatures

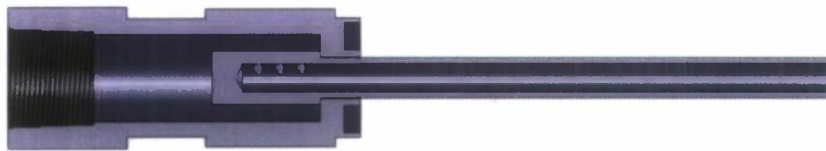


Fig. 4. Cut-away schematic of injector element.

until as close to the injection block as possible. After the metering orifice, a large manifold block is used for the methane propellant with independent feed lines to the injector block. Ports for the methane alternate top and bottom in the injector block.

Jensen, Dodson and Claflin [9, 10] noted that temperature ramping was an effective means of rating the stability characteristics of LOX/methane combustion. Thus, as a means of causing instabilities in the chamber, the methane was reduced temperature. Special hardware was required to accomplish this series of testing.

In order to cool the methane gas down to the low temperatures required for testing ( $-70$  to  $-90^{\circ}\text{C}$ ), a special bath was designed for the methane circuit. The bath was a cryogenic tank filled with a specially formulated heat transfer fluid from Duratherm Corp. The fluid was formulated to remain in a low viscosity liquid state with high heat transfer characteristics even at reduced temperature. An emersion cooler (Haake EK-90) was then used to bring the heat transfer fluid down to  $-90^{\circ}\text{C}$ . Propellant lines from the methane manifold were then coiled through the bath to create a simplified heat exchanger. Additional jackets of  $\text{LN}_2$  maintained cooled methane temperatures to the injector block.

For cooled methane testing, the run valves for the methane circuit were located upstream of the methane manifold block and feed lines from the manifold were independently routed

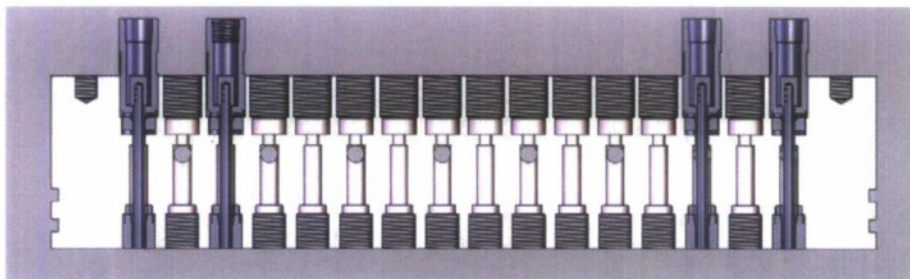


Fig. 5. Cut-view schematic of injector block showing 4 injector elements.

through the methane temperature bath to the injector block. Due to the increased length of line for the methane circuit, timing for the valves was adjusted to account for necessary line fill and pressurization. Temperature probes in the methane temperature bath and on two feed lines just at the feed line exit from the bath provided monitoring of methane temperature. A  $\text{LN}_2$  coil from the methane temperature bath to the injector block provided a trickle flow of liquid nitrogen to overcome temperature loss from the bath to the injector block.

#### 3.2.4 Nozzle and Nozzle Block

Nozzle elements were all of a singular design, fabricated from molybdenum, which could be mounted in a nozzle block permitting up to maximum of 8 nozzles elements. Each nozzle element was conical in design with a throat diameter of 5.44 mm (0.214 in.). When the nozzle element was inserted into the nozzle block, a flow passage was formed around the throat region nozzle element that was cooled using high pressure water as the coolant. When fewer than eight nozzle elements were being used, blanks with the same shape, but no throat cut-out, were inserted in empty spaces.

#### 3.2.5 Igniters

Two  $\text{GO}_2/\text{GH}_2$  igniters located on the side walls of the chamber provided uniform ignition across the chamber, and are the same as those discussed in other experiments [4, 5]. The igniters were fed from gas bottles independent of the main propellant feed system.

#### 3.2.6 High Frequency Pressure Transducers

PCB Electronics model 113A24 high frequency pressure transducers were used for high frequency pressure measurements in the chamber. Two sensors were used in the chamber, one mounted along the centerline of the chamber, the other near the side wall. Positions were chosen to measure the pressure oscillations the anti-nodes of the 1W and 2W modes (for the ease of the wall pressure transducer), as well as the node of the 1W mode and anti-node of the 2W mode (for the ease of the centerline pressure transducer). Figure 6 shows the positions of the sensors with respect to the mode shapes of the 1W and 2W modes. These sensors have a resonant frequency of 500 kHz and a pressure range of 0-1000 psi. Samples were taken at 100 kHz, so a maximum useful frequency range of 0-50 kHz was available. The transducers were mounted in water cooled jackets and recessed into the chamber wall to protect them from the hot combustion



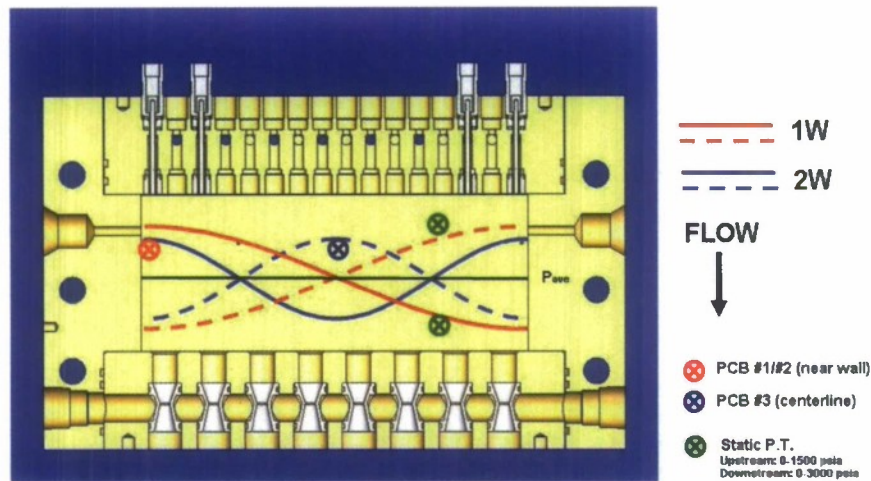


Fig. 6. Schematic of sensor positions with respect to mode shapes.

gases. Openings to the chamber were 1.59 mm (0.063 in.) diameter, 12.2 mm (0.480 in.) long for the centerline transducer, and 18.5 mm (0.730 in.) long for the wall transducer. Difference in measurement port lengths was due to the necessity of keeping the wall transducer recessed back further so the port opening could be as close to the side wall of the chamber as possible. Recesses were kept as much to a minimum as hardware allowed, in order to prevent spurious modes from being detected.

### 3.3 Test Conditions

#### 3.3.1 Basic Flow Conditions

Each injector element was designed based on a LOX flowrate of 0.057 kg/s (0.125 lbm/s) per element. The overall mixture ratio had an O/F = 3 ( $\phi = 1.33$ ), with methane ( $\text{CH}_4$ ) as the fuel. A total flowrate capability of 0.454 kg/s (1.00 lbm/s) of LOX flow was used. For reference, LOX/methane stoichiometric mixture ratio is O/F = 4. Table 1 lists the critical pressure and temperatures for LOX and methane for reference in evaluating the thermodynamic state of the propellants for the current studies. Nozzle elements could be altered to change the chamber pressure to the desired quantity.

Table 1. Table of critical temperature and pressure for LOX and methane.

Propellant	Critical Temp. (K [°F])	Critical Pressure (MPa [psia])
Liquid Oxygen (LOX)	154.6 [-181.4]	5.043 [731.4]
Methane	190.6 [-116.6]	4.599 [667.1]



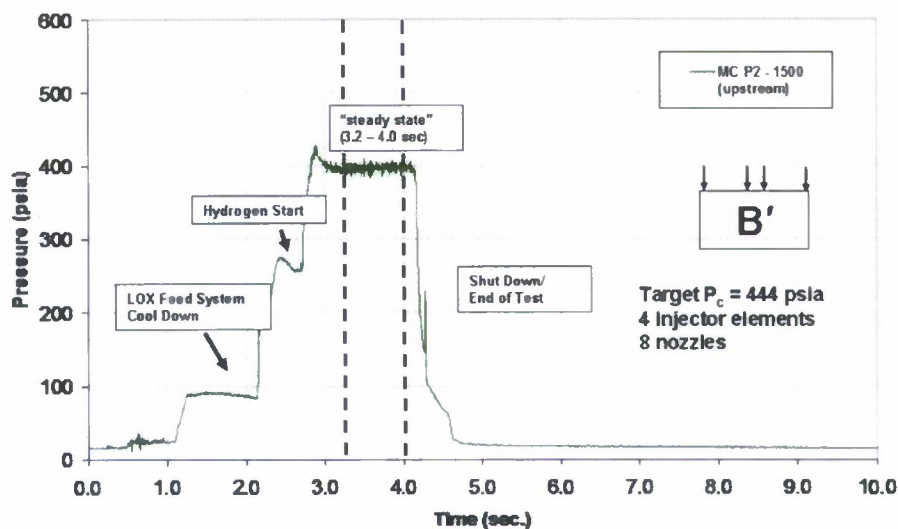


**Fig. 7.** Sample pressure trace for mean chamber pressure, indicating the steady state period used during test runs.

### 3.3.2 Basic Timing Sequence

The testing sequence for the rocket chamber consists of two stages, a start-stage, and a run-stage. The start stage was included to prove the ignition of the propellant flows as well as to ease the pressure shock to the system as it comes up to full pressure. Since methane is more difficult to successfully ignite, the start stage utilized hydrogen to ensure ignition, and then the hydrogen was shut off as methane was brought online during the transition to the run stage. Figure 7 shows a sample pressure trace for a typical test. Pressures are shown in psia, and are referenced to test run time.

## **4.0 Results and Discussion**

### **4.1 High Frequency Data Analysis Overview**

#### 4.1.1 Chamber Acoustic Characteristics

Before presenting the results, an overview of the analysis method for the high frequency pressure transducer measurements is presented. The modal calculations for the chamber are based upon solution of the wave equation for a rectangular cavity. The equation describing the acoustic modal frequencies of the cavity is given by:

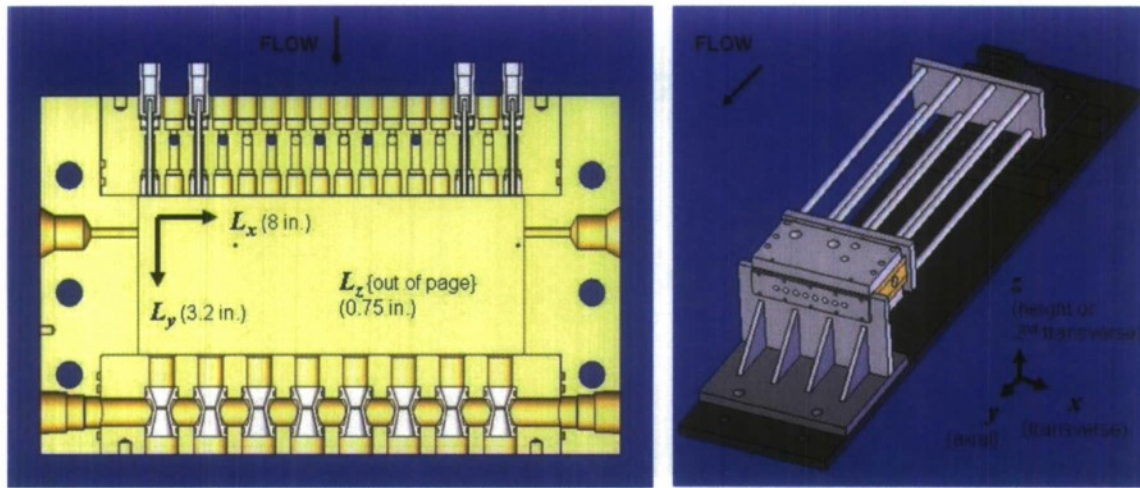


**Fig. 8.** Schematics illustrating coordinate system in describing acoustic modes of chamber. Left image: Section view of chamber with included dimensions. Right image: Schematic of chamber on test stand with included coordinate system.

$$f_{lmn} = \frac{a}{2\pi} \sqrt{\left(\frac{l\pi}{L_x}\right)^2 + \left(\frac{m\pi}{L_y}\right)^2 + \left(\frac{n\pi}{L_z}\right)^2} \quad [1]$$

where  $a$  is the acoustic velocity in the chamber,  $L_x$ ,  $L_y$ , and  $L_z$  are the dimensions of the chamber (see Fig. 8) and  $l$ ,  $m$  and  $n$  are the mode numbers corresponding to the  $x$ ,  $y$ , and  $z$  coordinates, respectively. In this analysis,  $l$  corresponds to the transverse mode related to  $L_x$ ,  $m$  to the longitudinal mode related to  $L_y$ , and  $n$  corresponds to the transverse mode related to  $L_z$ . The schematics in Fig. 8 illustrate the dimensions of the chamber ( $L_x$ ,  $L_y$ , and  $L_z$ ) with respect to the orientation of the chamber on the test stand. The left side image is a section view of the combustion chamber with dimensions included, whereas the right side image shows the rocket chamber assembly as placed on the test stand with the coordinate system shown. In these images,  $L_x$  is the width of the chamber (203 mm [8 in.]),  $L_y$  is the length (81.3 mm [3.2 in.]), and  $L_z$  is the height (19.1 mm [0.75 in.]). In referring to the modes of the chamber, the nomenclature for the modes in the transverse, longitudinal (or axial), and height (2nd transverse) dimensions are  $lW$ ,  $mL$ , and  $nH$ , respectively.

The dimensions of the rectangular chamber were selected such that the frequencies for the longitudinal and 2nd transverse modes were much greater than the 1W (transverse) mode. Table 2 lists the expected modal frequencies of the chamber assuming an equilibrium acoustic velocity (calculated from CEA [11, 12]) of 1277 m/s (4188 ft/s). CEA calculations for the

**Table 2.** Table of expected mode frequencies (Hz).

Mode No.	$x = 1$	$x = 2$	$x = 3$
$xW$	3141	6282	9423
$xL$	7853	15,706	23,559
$xH$	33,507	67,013	100,521

chamber with inputs of 888 psi chamber pressure and  $O/F = 3$  were used to determine the chamber gas acoustic velocity. The difference in acoustic speed for 222 psi tests is only 2% lower (1250 m/s), and thus does not significantly change expected mode frequencies (3078 Hz vs. 3141 Hz for 1W mode). Note that the frequencies for the 1L and 1H shown in Table 2 are well above the 1W and 2W modes of the chamber. Thus, the chamber is well suited to isolating the 1W and 2W modes for the present study. Given that fact and considering that the transverse modes are of primary interest, Equation 1 may be simplified to a 1-D equation, given by:

$$f_l = \frac{a}{2} \left( \frac{l}{L_x} \right) \quad [2]$$

It was observed during testing that the predicted modal frequency response did not match exactly with the frequencies given in Table 2. However, the frequencies were consistently shifted from equilibrium calculations to slightly lower values (e.g. 2500-2700 Hz as compared to the CEA predicted 3141 Hz). While the exact cause of this difference is unknown, departures from a uniform gas temperature field in the chamber and reduced  $c^*$  efficiencies ( $\eta_{c^*} < 1$ ) are suspected as reasons for reduced gas temperature in the combustion chamber and thus the observed lower frequency response.

#### 4.1.2 Power Spectrum Density Overview

Since the modal response of the chamber is frequency dependent, a method is needed to analyze from the high frequency signal measured in the time domain and transform it to the frequency domain. In the current study, the high frequency pressure signal is transformed into a Power Spectrum Density (PSD) plot. The PSD is related to the Fourier transform as shall be discussed next.

The most common and readily available method for this frequency analysis is the fast Fourier transform (FFT). The Fourier transform (FT) is given by:



$$\hat{f}(\omega) = \frac{1}{\sqrt{2\pi}} \int_{-\infty}^{\infty} f(t) e^{-i\omega t} dt \quad [3]$$

where  $f(t)$  is the value of the function (or signal) in the time domain where  $t$  is time,  $i$  is the imaginary number ( $\sqrt{-1}$ ),  $\omega$  is the angular frequency ( $\omega = 2\pi f$ ), and  $\hat{f}$  is the value of the function (or signal) transformed into the frequency domain.

The fast Fourier transform is the discretized form of the FT, written to take advantage of a computer's computational abilities and the nature of a discretized sample. Its form is given by:

$$X(k\Delta f) = \sum_{n=0}^{N-1} x(n\Delta t) e^{-i(2\pi k\Delta f)(n\Delta t)} \quad k = 0, 1, 2, \dots, N-1 \quad [4]$$

Here,  $X$  and  $x$  are the values of the function in the frequency and time domains, respectively.  $N$  is the total number of data points to be sampled over some time interval, where  $N$  is restricted to powers of 2.  $\Delta t$  is the increment of time, or sampling period (1/sampling rate). Both  $k$  and  $n$  are indices used in the summation.  $\Delta f$  is the frequency resolution, defined as the sampling frequency divided by the total number of samples,  $N$ .

Related to the Fourier transform, the power spectrum density (PSD) is a measure of how the power of a signal is distributed in the frequency domain. The power spectrum of a time dependent signal,  $f(x)$ , is given by:

$$S_{xx}(f) = X^*(f)X(f) = |X(f)|^2 \quad [5]$$

where  $X(f)$  is the Fourier transform of  $f(x)$  and  $X^*(f)$  is the complex conjugate of  $X(f)$ . Thus a plot of the power spectrum with respect to frequency is termed the power spectrum density. Integrating the power spectrum over the entire frequency domain gives the total intensity (expressed as  $\text{psi}^2/\text{Hz}$ ), or total variance ( $\sigma_{tot}^2$ ), of the entire signal, as expressed in Eq. 6.

$$\sigma_{tot}^2 = \int_{-\infty}^{\infty} |\hat{f}(\omega)|^2 d\omega \quad [6]$$

Integrating Eq. (4.6) from  $a$  to  $b$  as opposed to the entire domain gives the intensity of the signal between the frequencies of  $a$  and  $b$ .

#### 4.1.3 Power Spectrum Density Analysis

Because of the properties of Eq. 6, the PSD provides an effective means of analyzing the high frequency data. Integrating the PSD over the frequency range between  $f_1$  to  $f_2$  gives the intensity, also called the variance ( $\sigma^2$ ), of the signal within that frequency band. As noted in the



previous section (4.1.2), this is related to the pressure oscillation amplitude within this frequency band. Taking the square root of the variance then gives the root mean squared amplitude of the pressure oscillations ( $P'_{rms}$ ) within the desired frequency band. Multiplying the rms pressure oscillation amplitude by  $2\sqrt{2}$  yields the peak-to-peak amplitude of the pressure oscillations ( $P'_{p-p}$ ). It is then possible to relate the amplitude of pressure oscillations within a given frequency band relative to mean chamber pressure ( $P'_{p-p}/P_c$ ).

A set of virtual instrument (VI) written for the LabVIEW software provides a method for quickly obtaining the PSD of the high frequency pressure signal. By measuring the rms and peak-to-peak amplitudes of modal frequencies in the signal, and normalizing by mean chamber pressure, the mean instability level (defined here as  $P'_{p-p}/P_c$  and expressed as a percentage) can be determined. This level is expressed as a percentage of the mean chamber pressure for a given mode over any time interval of interest. The program can also be used to obtain an array of PSD variance and peak-to-peak pressure amplitude for a given frequency band as a function of time. Thus a plot of the peak to peak pressure amplitude versus time can be obtained. By comparing plots from different tests where conditions such as injector element placement, flow conditions and nozzle element placement were changed, stability characteristics may be obtained based on these changes in test conditions.

## **4.2 Chamber Response**

### **4.2.1 Acoustic Response Studies**

The initial set of experiments conducted in the rectangular rocket chamber focused on measuring the chamber frequency response as a function of injector placement and chamber pressure. This series of experiments measured the acoustic response to determine whether spontaneous combustion instability could be observed, as no external methods were used to excite an instability level in the chamber. By placing injectors at pressure anti-nodes, it was expected that instabilities could be readily generated as compared to those tests where injectors were placed at pressure nodes. It could then be observed whether spontaneous instabilities occurred within the chamber or not.

As discussed in Sec. 4.1.2, the primary method of analysis of the high frequency pressure signal was the use of the PSD. Through the PSD, it was possible to identify which modes were active in the chamber, and the relative amplitude of those signals. Figure 9 shows a sample PSD

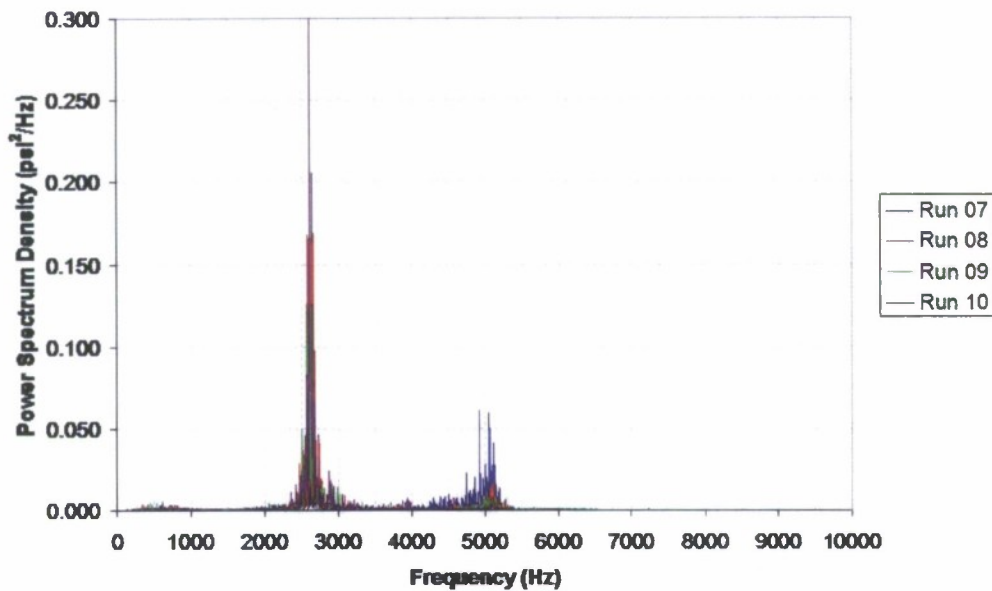
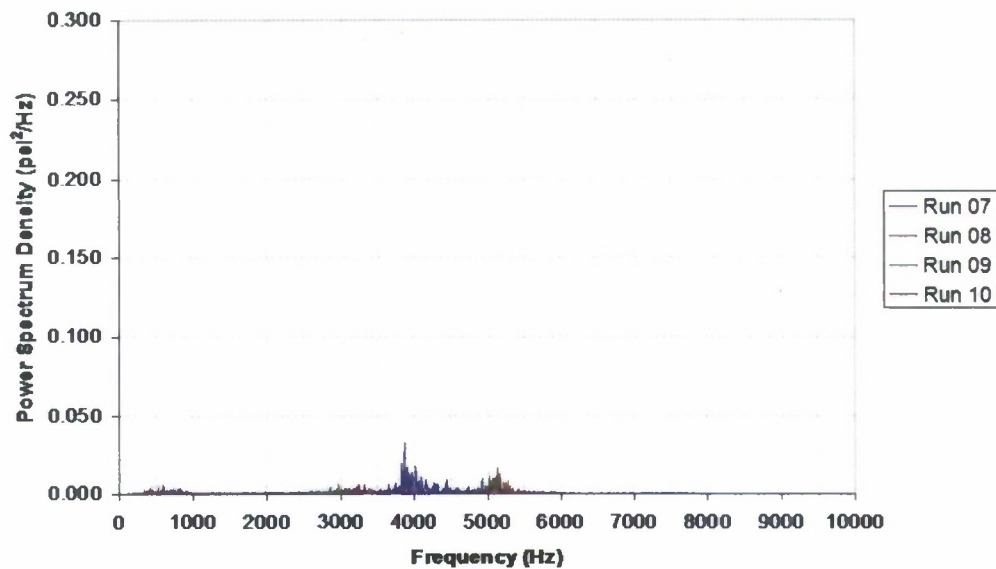


Fig. 9. PSD plot of wall transducer for 2 injector elements at the walls (Pos. 1 and 16),  $P_c = 222$  psia.

plot of the pressure transducer located near the wall (ref. Fig. 6 for position of the pressure transducer) for the case of two injectors located at positions 1 and 16 (ref. Fig. 3) and a target chamber pressure of 1.53 MPa (222 psi). The PSD shown was taken for  $2^{14}$  data points (16384 data points or 0.16 s of steady state portion of the pressure signal). In this figure the x-axis is frequency, whereas the amplitude (y-axis) indicates the PSD amplitude ( $\text{psi}^2/\text{Hz}$ ). Figures 9 (for the wall pressure transducer) and 10 (for the centerline pressure transducer) both have the 1W and 2W modes at approximately 2500 Hz and 5000 Hz, respectively. For comparison, the ideal modal frequencies based on equilibrium conditions are 3101 Hz and 6022 Hz for the 1W and 2W modes, respectively. Departures from these ideal frequencies are likely due to differences in gas temperature within the chamber, as evidenced by the approximate  $c^*$  efficiencies which ranged from 70-102% for all tests conducted. The mean and median values of  $c^*$  for all tests conducted were both 91%. It is also clear that the 1W mode PSD amplitude is quite strong compared to the 2W mode PSD amplitude, indicating that most of the acoustic energy is present in the 1W mode.

By comparison, Fig. 10 shows an example of the PSD for the same test runs, for the centerline pressure transducer. The axes of the plot are the same as previously described, and the data sample size is the same. For this case, it is noted that the 1W mode is significantly reduced



**Fig. 10.** PSD plot of centerline transducer for 2 injector elements at the walls (Pos. 1 and 16),  $P_c = 222$  psia.

compared to the wall pressure transducer plot (Fig. 9). This is expected, as the 1W mode exhibits a pressure node at the centerline position.

From observation, it is noted that the amplitude of the 2W mode is not the same for the wall and centerline transducers, despite the symmetric nature of the 2W mode. Ideally, these amplitudes should be the same, and no source for this disparity has been identified. One possible explanation, however, is due to local differences in the gas temperature and composition causing local differences in acoustic properties and modal characteristics, although it is not possible from the data to confirm this. Based on static pressure transducer measurements, the actual chamber pressure was lower than the target condition, with an approximate  $c^*$  efficiency for this test condition of 98%. It is worth noting here that acoustic characteristics of the chamber are assumed on linear acoustic theory in a confined duct with no additional openings.

#### 4.2.2 Burst Phenomenon

Upon further examination of the raw high frequency pressure signals, it was observed that pressure oscillations in the chamber grew and decayed in amplitude quickly. These oscillations occur in random patterns throughout the test sequence and are hereafter referred to as “burst” phenomenon. Figure 11 illustrates the burst phenomenon within the chamber. The main plot of the figure shows a sample time trace, in this case for a two injector case (Pos. 1,16), four nozzles,

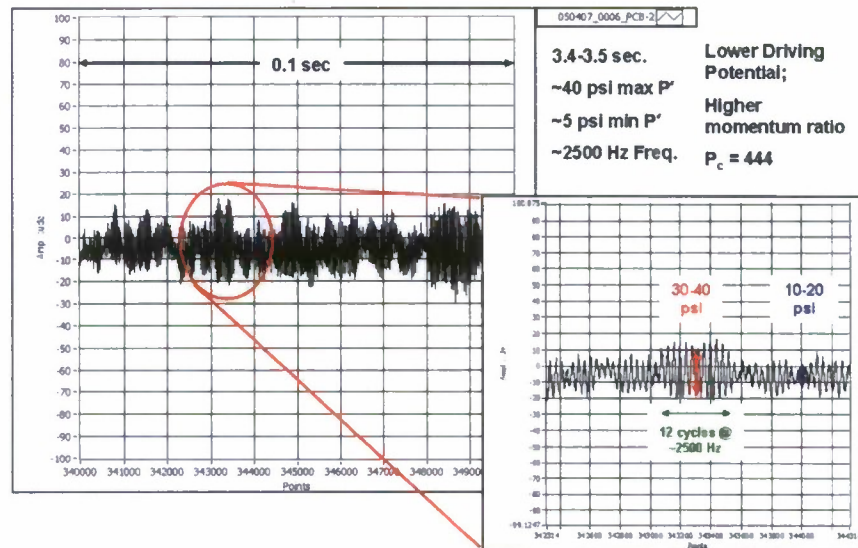


**Fig. 11.** Illustration of burst phenomenon during test series.

target  $P_c = 444$  psia, with 0.143 in. I.D. annuluses (higher momentum ratio). The y-axis shows the amplitude of the pressure signal above mean chamber pressure, whereas the x-axis shows the data point number of the cycle. The x-axis is also representative of the time scale, since the sample rate was  $1 \times 10^5$  pts./s. To obtain the time scale, simply divide the point number by the sample rate. Thus, while the x-axis begins at 340000, this is analogous to 3.4 s. The main plot of the figure represents 0.1 s worth of data from the steady state portion of the rocket firing. At this scale, the burst phenomenon of the instability is evident. The inset of the figure is a zoomed in portion of the main graph, showing a segment approximately 0.02 s in duration. The 1W mode frequency is clearly evident in this inset. Examination of the figure shows that 1W mode oscillation amplitudes ( $P'_{p-p}$ ) during this segment grow from approximately 10 psi ( $\sim 2.5\% P'_{p-p}/P_c$ ), to a level of 40 psi ( $\sim 10\% P'_{p-p}/P_c$ ). The pattern of the bursts is random in nature. In the inset, the main burst shown is approximately 12 cycles in duration, with a predominant 1W mode frequency of  $\sim 2500$  Hz.

#### 4.2.3 Short-Time Fourier Analysis

Because of the burst nature of the instabilities in the chamber, the previous method of examining instabilities in the chamber as an average segment (ref. Sec. 4.2.1) was not sufficient to fully describe the instability level in the chamber. Thus, a short-time Fourier analysis (STFA) was performed to provide a time history of the instability level in the chamber. In this method, a



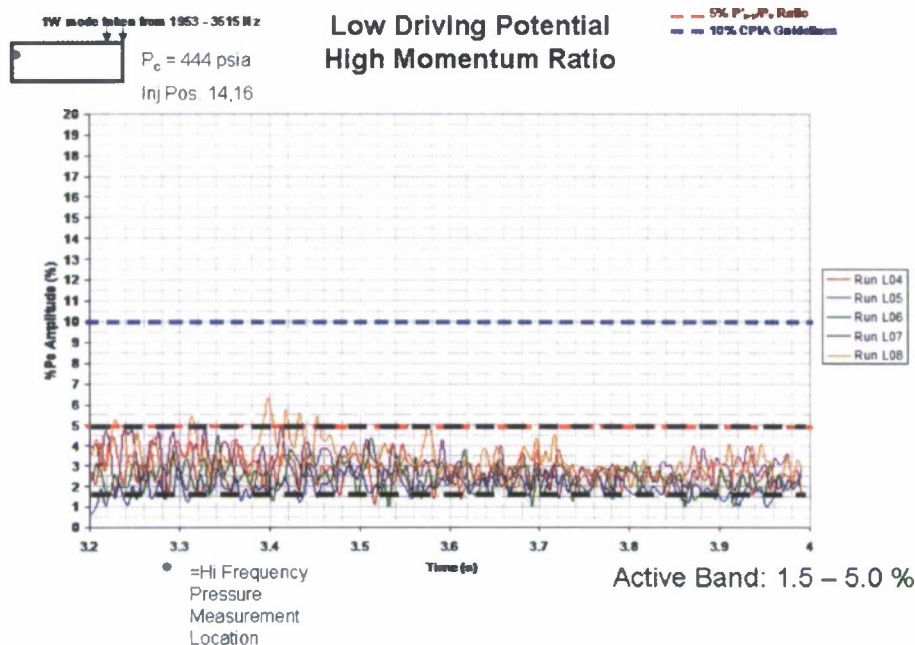


Fig. 12. Example plot of 1W mode vs. time.

FFT was run on the signal for a short period of time (in this case 512 data points), then the FFT analysis advanced forward by 500 data points, providing a small overlap between subsequent FFTs to a new segment of signal. Throughout the analysis, the variance and peak-to-peak oscillation amplitude is measured for a particular mode of interest (either the 1W or 2W mode). Thus, a running value of the variance and instability level of particular modes as a function of time can be obtained. Figure 12 shows an example of a 1W mode plot obtained by STFA. In Fig. 12, the y-axis is the instability level ( $P'_{p-p}/P_c$ ) and the x-axis is the runtime (note steady state chamber pressure data occurs from 3.2 to 4.0 seconds during the test sequence). Several runs at the same test conditions are shown. The blue dashed line in the figure represents the 10% instability level, whereas the red dashed line represents the 5% instability level, shown for quick reference. Black dashed lines bracket the approximate maximum and minimum instability levels of the particular test condition. Thus, STFA plots for various modes may be quickly compared to see how changes in test conditions (such as injector placement) affect instability levels.

#### 4.2.4 Temperature Ramping Studies

Since the pulsation device did not induce instability levels ( $P'_{p-p}/P_c$ ) of the magnitude expected, other methods of driving instabilities were investigated. In particular, following the work of Jensen, *et al.* [9, 10], reduction of the methane gas temperature appeared a possible mechanism for inducing instabilities within the combustion chamber and was of particular interest for this study. The method utilized in the present work for reducing methane gas temperature used a simple thermal heat exchanger. Based on the studies by Jensen, *et al.*, [9], it was determined that a target methane gas temperature of  $-90^{\circ}\text{C}$  would be sufficient for inducing instabilities. Tests were conducted for both ambient (room temperature) and cooled methane runs for the same chamber conditions. Figure 13 shows a sample 1W mode plot for a cooled methane test, whereas Fig. 14 shows a 1W mode plot for an ambient temperature test. The y-axis and x-axis are the same as those discussed for Fig. 12. The tests shown were for four injector elements (Pos. 13, 14, 15, 16) with eight nozzles ( $P_c = 444$  psia), as illustrated by the graphic in the upper left corner. It should be noted that the mean methane gas temperature, measured just upstream of injection was  $-70$  to  $-100^{\circ}\text{F}$  ( $-56$  to  $-73^{\circ}\text{C}$ ) for the cooled studies and

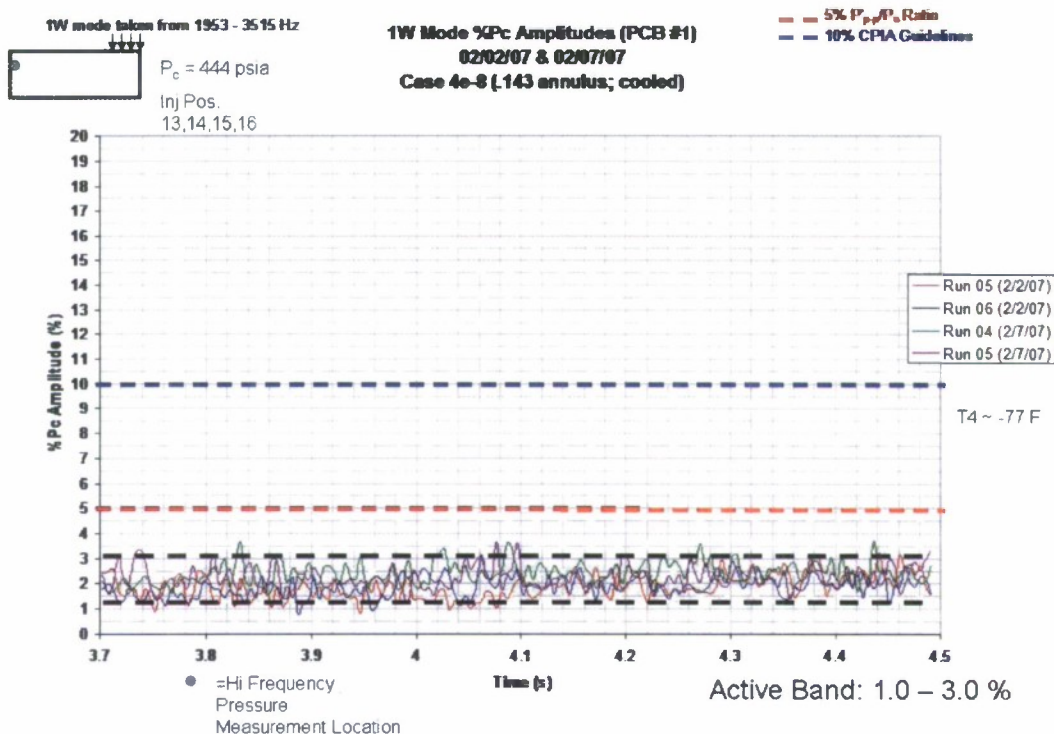


Fig. 13. Example plot of 1W mode vs. time for cooled methane tests.

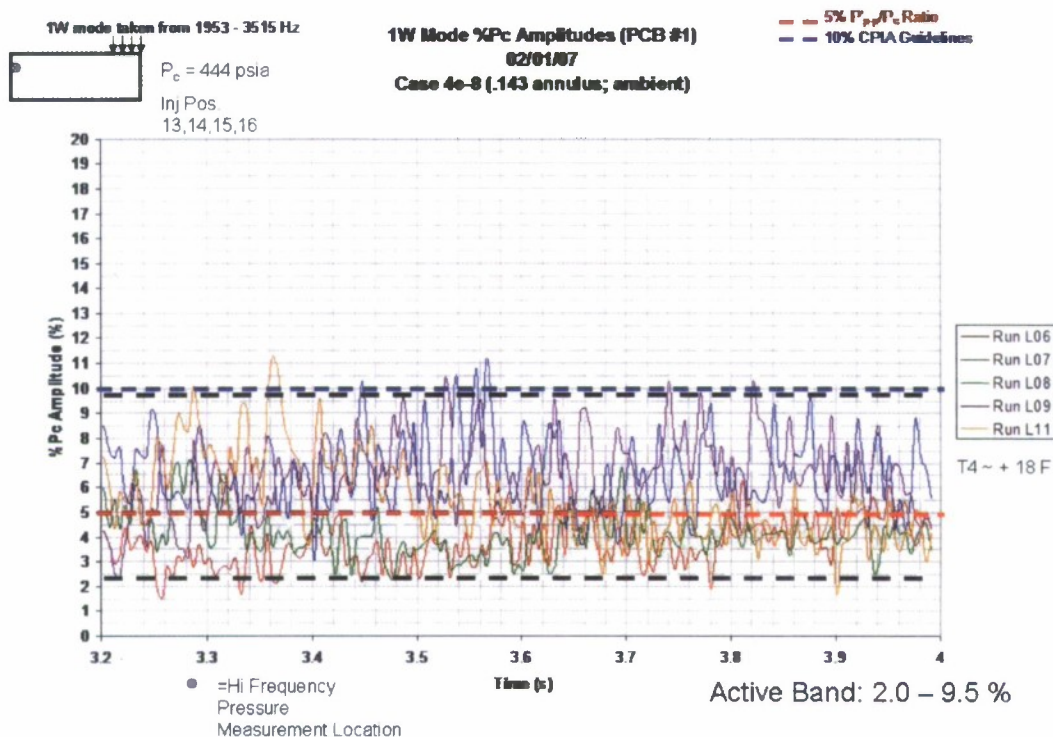
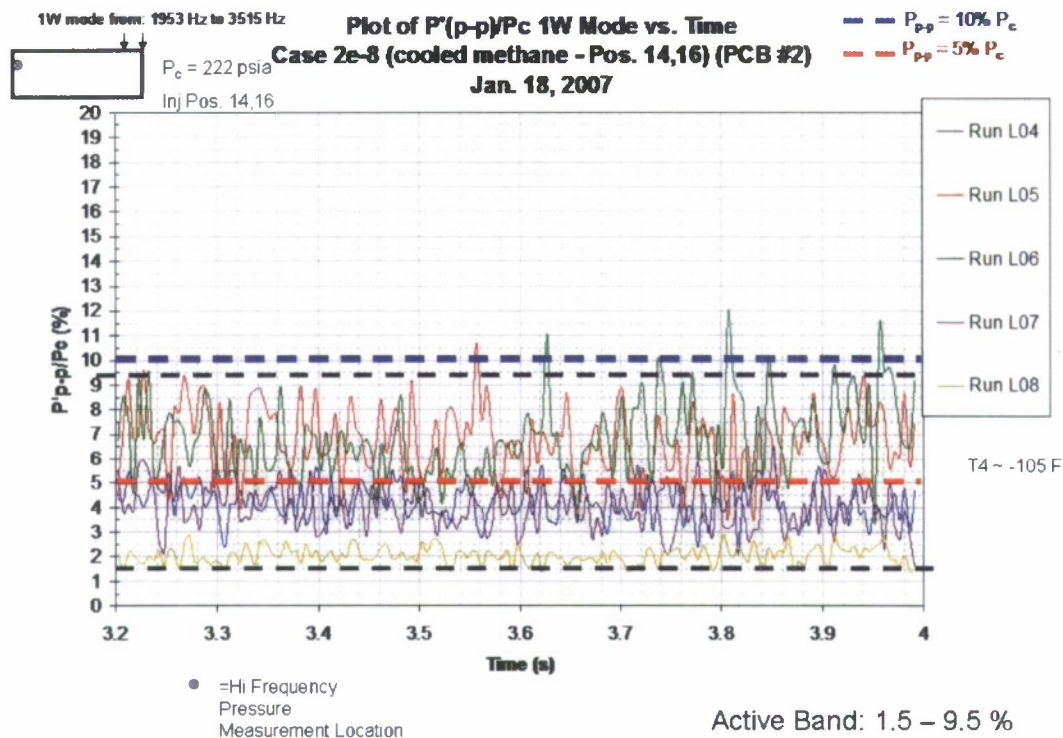


Fig. 14. Example plot of 1W mode vs. time for ambient temperature methane tests.

was -6 to +40°F (-21 to +4°C) for the ambient temperature studies. From these results, one major conclusion can be drawn. Despite evidence from Jensen, *et al.* [9] that cooled methane is a viable option for performing stability rating of a chamber, it was insufficient in the current studies to show any significant effect on the chamber. In fact, a few tests conducted with cooled methane exhibited even more stable operation than those with ambient temperature propellants (as shown in Figs. 13 and 14). However, it is unclear as to why this current study shows results in contradiction with those of Jensen, *et al.* [9]. However, there are some key differences between the tests. One, Jensen, *et al.* [9] note that the instabilities observed during the cooled tests were not necessarily 1W modes, but rather an odd mode that did not correspond to chamber acoustics. Finally, the work by Jensen, *et al.* [9] utilized shear coaxial injectors while the current work used swirl coaxial injectors. While similar in concept, there are inherent differences between the two injector types including mixing and atomization properties. Jensen, *et al.* [9] note that the odd mode may be related to organ pipe modes of the fuel annulus with the combustion chamber. Thus, a meaningful one-to-one comparison between the current and previous bodies of work may not be appropriate.





**Fig. 15.** Example plot of 1W mode vs. time for cooled methane tests-showing different instability levels for similar test conditions.

One of the most common problems with combustion instability is the elusive and unpredictable nature of occurrences. Simply having conditions which favor occurrences of instabilities does not guarantee that an event will occur. Thus, as noted by Sutton [13], it may take numerous tests to detect a potentially catastrophic condition. The current series is no exception to this trend. While most test conditions conducted in the current studied showed similar behavior run to run, a few test conditions showed dramatically different behavior from run to run. Figure 15 shows an example of a test condition whose individual runs exhibited dramatically different results. The figure, which is a plot of the 1W mode similar to those discussed previously, shows 5 test runs for the chamber operating with two injector elements located at the wall (Pos. 14 and 16), eight nozzles, a target chamber pressure of  $P_c = 222$  psia, with cooled methane propellant ( $T_{inj} = -105^\circ\text{F}$ ). Of the five runs shown, two had rather significant instability levels greater than 5%, two had moderate levels between 3-5%, and one had negligible instability levels.



**Table 4.3.** Summary of test conditions showing differing instability levels in chamber.

Run #	Chamber Pressure MPa [psia]	Methane T <sub>4</sub> °C [°F]	LOX T <sub>4</sub> °C [°F]	O/F	Instability Level (%) (P' <sub>p-p</sub> /P <sub>c</sub> )
4	1.43 [207.9]	-73.5 [-100.3]	-169.9 [-273.8]	2.93	4.22
5	1.45 [210.1]	-75.6 [-104.0]	-172.3 [-278.1]	2.99	6.76
6	1.45 [210.4]	-76.2 [-105.1]	-173.9 [-281.0]	3.04	6.80
7	1.46 [211.1]	-76.7 [-106.0]	-174.4 [-282.0]	3.04	3.97
8	1.45 [210.7]	-76.9 [-106.4]	-174.7 [-282.5]	3.04	2.05

The tests were all conducted on the same day, under similar flow conditions, with no significant departures from target flow conditions. Actual chamber pressure for these tests were approximately 210 psia on average, with an approximate  $c^*$  efficiency of 90%. The tests, in order, had instability levels of 4.22, 6.76, 6.80, 3.97, and 2.05% mean instability level( $P'_{p-p}/P_c$ ). Table 3 lists the significant flow conditions for these tests.

### 5.0 Summary and Conclusions

Studies were conducted using a rectangular rocket chamber burning LOX/methane to investigate the effect of methane temperature on combustion instability initiation. LOX centered swirl injector elements were utilized in all the tests. Chamber pressures between 222 and 444 psia were studied by varying the number of injector elements, injector placement and methane temperature. Hot-fire tests with injector elements positioned near the pressure anti-node of the first transverse mode exhibited the highest pressure oscillations.

The methane propellant temperature was varied over a temperature range from -70 to -100°F (-56 to -73°C) for the cooled studies and from -6 to +40°F (-21 to +4°C) for the ambient temperature studies. The results obtained from monitoring the pressure oscillations using high speed pressure transducers indicated no difference between the cooled methane test cases as compared to the ambient temperature test cases. Pressure oscillations were observed for some tests to be as high as 10% of the mean chamber pressure for both the cooled and ambient temperature cases. However, repeated tests at the same conditions showed the magnitude of the observed pressure oscillations varied from 2-10%. Thus, the high variability in the observed pressure oscillations appears to have no relationship to the temperature of the methane propellant.

## 6.0 References

- [1] "JANNAF Liquid Rocket Combustion Instability Panel Research Recommendations," Klem, Mark D. (NASA Lewis Research Cent) Source: NASA Technical Memorandum, n 103653, Nov, 1990, p. 11.
- [2] Hulka, J. and Hutt, J. J., "Instability Phenomena in Liquid Oxygen/Hydrogen Propellant Rocket Engines," Liquid Rocket Engine Combustion Instability, V. Yang and W. Anderson (Eds.), Chapter 2, Vol. 169, Progress in Astronautics and Aeronautics, 1995.
- [3] Liquid Propellant Rocket Combustion Instability, NASA SP-194, D. T. Harrje and F. H. Reardon (editors) 1972.
- [4] Moser, M. D., "Flowfield Characterization in a Uni-Element Rocket Chamber," Ph.D. Thesis, The Pennsylvania State University, 1995.
- [5] Foust, M. J., "An Experimental Investigation of Gaseous Propellant Rocket Injectors Using Raman Spectroscopy," Ph.D. Thesis, The Pennsylvania State University, 1997.
- [6] Lehman, M. K., "Mixing and Reaction Processes in Rocket Based Combined Cycle and Conventional Rocket Engines," Ph.D. Thesis, The Pennsylvania State University, 2000.
- [7] Marshall, W. M., "Experimental Studies of Combustion Instabilities in a Multi-element Rectangular Rocket Chamber," Ph.D. Thesis, The Pennsylvania State University, 2008
- [8] Santoro, R. J., Pal, S., Woodward, R. D., and Schaaf, L., "Rocket Testing at University Facilities," AIAA 2001-0748, *39th AIAA Aerospace Sciences Meeting and Exhibit*, Reno, NV, January 8-11, 2001.
- [9] Jensen, R. J., Claflin, S. E., and Dodson, H., "Liquid Oxygen/Methane Combustion Instability Investigation," *Combustion Instabilities Driven by Thermo-Chemical Acoustic Sources - Presented at the Winter Annual Meeting of the American Society of Mechanical Engineers*, San Francisco, CA, December 10-15, 1989.
- [10] Jensen, R. J., Dodson, H. C., and Claflin, S. E., "LOX/Hydrocarbon Combustion Instability Investigation," National Aeronautics and Space Administration, NASA CR-182249, 1989.

- [11] Gordon, S. and McBride, B. J., "Computer Program for Calculation of Complex Chemical Equilibrium Compositions and Applications: I. Analysis," NASA Reference Publication 1311, 1994.
- [12] McBride, B. J. and Gordon, S., "Computer Program for Calculation of Complex Chemical Equilibrium Compositions and Applications: II. Users Manual and Program Descriptions," NASA Reference Publication 1311, 1996.
- [13] Sutton, G.P., "History of Liquid Propellant Rocket Engines in the United States," *Journal of Propulsion and Power*, Vol. 19, No. 6, November-December 2003, pp. 978-1007.

### **7.0 Personnel Supported**

Robert J. Santoro, P.I.  
 Sibtosch Pal, Senior Research Associate  
 Roger Woodward, Research Associate  
 Larry Schaaf, Research Support Technologist  
 William Marshall, Graduate Research Assistant  
 David Lyons, Graduate Research Assistant  
 Michelle Christensen, Graduate Research Assistant  
 Justin Locke, Graduate Research Assistant

### **8.0 Publications**

- [1] Combustion Instability Studies in a Rectangular Rocket Chamber, AIAA 2008-4656, William M. Marshall, Sibtosch Pal and Robert J. Santoro, 44th AIAA Joint Propulsion Conference & Exhibit, Hartford, CT, July 20-23, 2008
- [2] Experimental Study of Transverse Combustion Instabilities in a Multi-Element, Rectangular Rocket Chamber, AIAA 2007-5588, William M. Marshall, Sibtosch Pal, Roger D. Woodward, and Robert J. Santoro, 43rd AIAA Joint Propulsion Conference & Exhibit, Cincinnati, OH, July 1-11, 2007.
- [3] Combustion Instability Studies Using Gaseous Methane and Liquid Oxygen, William M. Marshall, Sibtosch Pal, Roger D. Woodward, and Robert J. Santoro, 42nd AIAA Joint Propulsion Conference, Sacramento, CA, July 10-13, 2006.

## **9.0 Interactions/Transitions**

### **9.1 Participation/presentation at meeting, conferences, workshops and seminars, etc.**

AFOSR/NASA Office of Chief Engineer Joint Contractors/Strategic Planning Meeting in Chemical Propulsion, July 2008 To July 2008, Presenter (2 talks).

International Workshop on Combustion-Generated Fine Carbon Particles, May 2007, University of Naples Federico II, Anacapri, Italy, Invited Speaker.

Workshop on the Future of Modeling and Simulation for Combustion Applications, sponsored by DoE, NETL and AFR, February 2006, Pittsburgh, PA, Invited participant.

### **9.2 Consultative and advisory functions to other laboratories and agencies**

None

### **9.3 New discoveries, inventions and patent disclosures**

None

## **10. Honors/Awards**

R. J. Santoro, Fellow of the American Society of Mechanical Engineers